RESEARCH PAPER

Polar Coordinate Mhd Modelling of Plasma–Dust Accretion Around Black Holes with Full Gravitational Components

S. Kavitha[1], S. Sugarami S[2]

[1,2] Department of Mathematics, Annamalai University, Annamalainagar – 608002, India.

[1] Email: kavitha_aucdm@yahoo.com

[2] Email: sugaramir21@gmail.com

Received: 20th Feb, 2026 | **Revised:** 4th Mar, 2026 | **Accepted:** 25th Mar, 2026 | **Available Online:** 10th Apr, 2026

1

A two-dimensional viscous accretion flow around a black hole is studied in the presence of electric and magnetic fields, gravity acting in the radial direction (g sin θ) and azimuthal direction (−g cos θ), and dust impurities. The flow is modelled in polar coordinates using the Navier–Stokes equations coupled with a reaction–diffusion equation for impurity concentration. The governing system includes the continuity equation, radial and azimuthal momentum equations, and the impurity transport equation, incorporating viscous stresses, Lorentz forces, and chemical reaction effects. Key dimensionless parameters—Hartmann number (M), Electric field number (Ee), Reynolds number (Re), Peclet number (Pe), and Reaction rate constant (Kc)—are analysed for their effects on velocity distribution, impurity concentration, accretion rate, and jet formation. The model captures essential physical features such as radial inflow, azimuthal rotation, shock structures, and magnetic reconnection zones, providing insight into the combined influence of electromagnetic forces, gravity, and dust impurities on black hole accretion flows.

Keywords: Accretion flow; Black hole; Magnetohydrodynamics (MHD); Gravity; Lorentz force; Impurities; Reaction–diffusion; Jet formation.

How to cite this article: Kavitha S, Sugarami S. Polar Coordinate Mhd Modelling of Plasma–Dust Accretion Around Black Holes with Full Gravitational Components. Int J Drug Deliv Technol. 2026;16(29s):1040-1051. DOI: 10.25258/ijddt.16.29s.129

Source of support: Nil.

Conflict of interest: The authors declare no conflict of interest.

1. INTRODUCTION

Accretion flow around black holes represent one of the most fundamental and challenging problems in modern astrophysics, owing to the strong interplay between gravitational forces, magnetic fields, electric fields, viscous stresses, and multi-species plasma interactions. When matter falls into the deep gravitational potential well of a black hole, the flow becomes highly dynamic and nonlinear, evolving through the combined action of radial inflow, rotational shear, turbulence, and magnetohydrodynamic (MHD) instabilities. Classical accretion disk theory, initiated by Shakura and Sunyaev (1973), demonstrated that angular momentum transport is a crucial mechanism enabling accretion. Later, the discovery of the magneto rotational instability (MRI) by Balbus and Hawley (1998) provided the fundamental physical explanation for turbulence-driven momentum transport in accretion flows.

In the vicinity of a black hole, gravity acts not only in the radial direction but also contributes significantly to the angular direction, generating sin θ and cos θ-dependent components that modify both the radial and azimuthal momentum balances. These gravitational components influence the structural evolution of the disk, the velocity shear distribution, and the formation of boundary layers. Moreover, the strong curvature of spacetime further magnifies the influence of gravity on plasma dynamics, particularly near the innermost stable circular orbit (ISCO). Although full general-relativistic magnetohydrodynamic (GRMHD) models exist (Koide et al., 1999), analytical and semi-analytical models remain essential for isolating and understanding the fundamental physical mechanisms governing accretion and jet formation.

Electromagnetic forces play a crucial role in controlling disk stability and energy extraction. Magnetic tension, magnetic pressure, and induced electric fields modify the angular momentum profile and can drive powerful outflows and jets. Lorentz forces influence both the magnitude and direction of plasma flow, particularly in the radial direction where they strongly modify the accretion velocity. Previous studies by Bisnovatyi-Kogan and Lovelace (2001),

Shadmehri (2004), and Ghosh and Chakrabarti (2018) have demonstrated that MHD-driven processes determine shock formation, magnetic reconnection regions, and energy dissipation within accretion disks. These effects are central to understanding jet launching mechanisms, which require a delicate balance between rotation, magnetic forces, and inflow velocity.

In realistic astrophysical environments, the accreting material is not a pure ionized gas but contains dust grains, molecular impurities, metallic contaminants, and other reactive species. Dust–plasma interactions significantly alter the mass density, ionization state, and effective viscosity, as shown in dusty plasma studies by Pandey and Vladimirov (2007), Laibe and Price (2012), and Matarrese and Mohayaee (2002). Impurities undergo diffusion, advection, and chemical transformation processes that are well described by reaction–diffusion systems (Murray, 2003). Understanding impurity transport is essential because dust grains absorb radiation, modify cooling rates, and influence the onset of instabilities. In strongly magnetized environments, dust particles may acquire electric charge, further enhancing electromagnetic coupling and altering the overall flow structure.

In many astrophysical and laboratory plasma systems, accretion or flow occurs through porous channels or permeable boundaries. Such situations are effectively modeled using the Beavers–Joseph slip boundary condition (Beavers and Joseph, 1967), which introduces a relationship between boundary shear stress and velocity slip at porous interfaces. Incorporating this boundary condition provides a more realistic representation of plasma–dust flow near disk surfaces or porous media interfaces, where partial slip and boundary-layer distortions significantly affect angular momentum transport.

The governing system considered in the present study consists of: (i) the continuity equation, (ii) the radial momentum equation incorporating viscous, gravitational, and electromagnetic forces, (iii) the azimuthal momentum equation including shear, rotation, and angular gravity effects, and (iv) the impurity concentration equation modeled as a reaction–diffusion process. These equations are formulated in two-dimensional polar coordinates (r, θ), allowing accurate representation of rotational effects, curved geometry, and directional gravity.

The full nonlinear MHD system is analytically intractable in its complete form. To overcome this difficulty, a perturbation technique is employed. This method decomposes each flow variable into a steady base component and a small perturbation component. Classical works by Nayfeh (1973) and Bender and Orszag (1999) provide the mathematical foundation for such asymptotic and perturbation-based analyses. Linearization about the base state yields a set of linearized perturbation equations that describe the response of velocity, impurity concentration, and electromagnetic fields to small disturbances.

This approach enables a systematic investigation of the influence of key nondimensional parameters, including the Hartmann number (M), Electric field number (Ee), Reynolds number (Re), Peclet number (Pe), and reaction rate constant (Kc). Through perturbation analysis, mechanisms responsible for flow destabilization, impurity accumulation, shock formation, and jet-like acceleration are identified. The combined action of radial gravity, angular gravity, electromagnetic forces, and porous boundary slip conditions produces a rich spectrum of flow behaviors, such as shear-layer formation, enhanced radial inflow, modification of angular velocity profiles, and variations in accretion rate.

The present work therefore develops a comprehensive mathematical and physical framework for analyzing two-dimensional plasma–dust accretion flow around a black hole under the combined influence of gravity, electric fields, magnetic fields, and reaction–diffusion mechanisms. The model provides a unified basis for exploring accretion dynamics, stability characteristics, and the emergence of high-energy astrophysical structures such as jets and magnetic reconnection zones.

2. MODEL FORMULATION

The accretion flow around a black hole is described using a two-dimensional polar coordinate system (r, θ). The radial velocity $v_r(r,\theta)$is directed inward toward the black hole, while the azimuthal velocity $v_\theta(r,\theta)$represents the orbital motion of the accreting matter within the disk. The gravitational acceleration $g$acts toward the black hole center and is resolved into radial and azimuthal components, $g\cos\theta$and $g\sin\theta$, respectively, in accordance with the flow geometry illustrated in the diagram.

Dust particles embedded within the accretion disk interact with the plasma and modify the local viscosity, effective density, and momentum transport mechanisms. As a result, the presence of impurities influences both the radial inflow velocity $v_r$and the azimuthal velocity v_θ. The governing equations of the flow consist of the continuity equation and the Navier–Stokes equations formulated in polar coordinates, with gravitational forcing terms $g\cos\theta$appearing in the

radial momentum equation and $g\sin\theta$appearing in the azimuthal momentum equation.

In addition to the hydrodynamic equations, the transport of dust impurities is modeled using a concentration equation that includes advection, diffusion, and reaction effects. The presence of a dust-rich layer introduces additional drag and reaction terms, representing the coupling between the fluid motion and impurity dynamics. These terms account for momentum exchange between the plasma and dust components, as well as chemical or physical transformation of impurities within the flow.

This mathematical framework provides a comprehensive description of the evolution of radial inflow, azimuthal shear, and dust-modified accretion dynamics around a black hole. The model captures the essential coupling between gravity, fluid motion, and impurity transport, forming the basis for subsequent perturbation analysis and numerical investigation of accretion flow behavior, as illustrated schematically in the corresponding diagram.

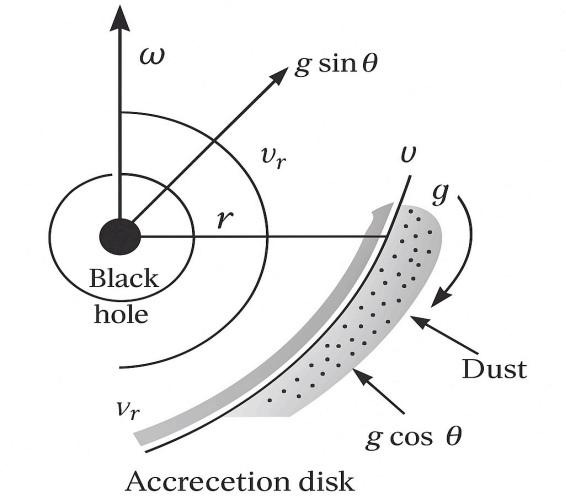

Figure 1. Schematic representation of plasma–dust accretion flow around a black hole in polar coordinates, illustrating the radial velocity v_r, azimuthal velocity v_θ, dust distribution within the porous layer, and the gravitational force components $g\sin\theta$(radial) and $g\cos\theta$(azimuthal).

Governing Equations

Continuity Equation

$$\frac{\partial\rho}{\partial t}+\frac{1}{r}\frac{\partial(r\rho v_r)}{\partial r}+\frac{1}{r}\frac{\partial(\rho v_\theta)}{\partial\theta}=0 \qquad (2.1)$$

Radial Momentum Equation

$$\rho\left(\frac{\partial v_r}{\partial t}+v_r\frac{\partial v_r}{\partial r}+\frac{v_\theta}{r}\frac{\partial v_r}{\partial\theta}-\frac{v_\theta^2}{r}\right)=-\frac{\partial p}{\partial r}+\mu\left[\frac{\partial^2 v_r}{\partial r^2}+\frac{1}{r}\frac{\partial v_r}{\partial r}-\frac{v_r}{r^2}+\frac{1}{r^2}\frac{\partial^2 v_r}{\partial\theta^2}-\frac{2}{r^2}\frac{\partial v_\theta}{\partial\theta}\right]+\rho eE_r+J_\theta B_z+\rho g\sin\theta \qquad (2.2)$$

Azimuthal Momentum Equation

$$\rho\left(\frac{\partial v_\theta}{\partial t}+v_r\frac{\partial v_\theta}{\partial r}+\frac{v_\theta}{r}\frac{\partial v_\theta}{\partial\theta}+\frac{v_r v_\theta}{r}\right)=-\frac{1}{r}\frac{\partial p}{\partial\theta}+\mu\left[\frac{\partial^2 v_\theta}{\partial r^2}+\frac{1}{r}\frac{\partial v_\theta}{\partial r}-\frac{v_\theta}{r^2}+$$

Impurity Concentration Equation (Reaction–Diffusion)

$$\frac{\partial c_i}{\partial t}+v_r\frac{\partial c_i}{\partial r}+\frac{v_\theta}{r}\frac{\partial c_i}{\partial\theta}=D\left[\frac{1}{r}\frac{\partial}{\partial r}\left(r\frac{\partial c_i}{\partial r}\right)+\frac{1}{r^2}\frac{\partial^2 c_i}{\partial\theta^2}\right]-Kc_i \qquad (2.4)$$

Here, $p$represents the fluid pressure, $E_r$denotes the radial component of the electric field, $\rho$is the fluid density, and $\mu$is the coefficient of viscosity. The externally applied magnetic field is assumed to act in the axial direction and is denoted by B_z, while $\rho_e$represents the electric charge density of the plasma. The impurity (plasma–dust) concentration is represented by c_i, with the assumption that $\beta\neq 0$for $i=1$, indicating the presence of reactive impurities.

To close the governing system, the Beavers–Joseph slip boundary condition is employed to account for boundary effects on the velocity field. This condition models partial slip at the porous boundary and captures the influence of boundary-layer dynamics on the accretion flow.

Boundary Conditions

The boundary conditions for the present problem are prescribed at the angular locations $\theta=0$, $\theta=2\pi$, and $\theta=-2\pi$.

At $\theta=0$, the no-slip condition is imposed on the velocity field, and the impurity concentration is assumed to have a small oscillatory perturbation:

$$v_r=0, v_\theta=0, c_i=c_0\,\varepsilon\,e^{i(\alpha r+\omega t)}, \text{at } \theta=0.$$

At $\theta=2\pi$, the Beavers–Joseph slip condition is applied to model the interaction between the free flow and the porous boundary. The azimuthal velocity and impurity concentration are prescribed as:

$$\frac{\partial v_r}{\partial\theta}=-\alpha_p\sqrt{k}\,(v_r-v_{rp}), v_\theta=v_{\theta1}, c_i = c_0\left(1+\varepsilon e^{i(\alpha r+\omega t)}\right), \text{at } \theta=2\pi.$$

Similarly, at $\theta=-2\pi$, the slip condition is retained with a different azimuthal velocity:

$$\frac{\partial v_r}{\partial\theta}=-\alpha_p\sqrt{k}\,(v_r-v_{rp}), v_\theta=v_{\theta2}, \text{at } \theta=-2\pi.$$

Here, $\alpha_p$denotes the slip coefficient, $k$is the permeability of the porous medium, and v_{rp}represents the seepage velocity within the porous layer.

Darcy's Law

The seepage velocity in the porous medium is governed by Darcy's law, given by:

$$v_{rp}=-\left(\frac{k}{\mu}\right)\frac{\partial p}{\partial r},$$

where $k$is the permeability of the porous medium and $\mu$is the dynamic viscosity of the fluid.

Non-dimensional Variables

In order to transform the governing equations into nondimensional form, the following dimensionless variables are introduced:

$$\tilde{r} = \frac{r}{l}, \tilde{t} = \frac{tv}{l}, \tilde{v}_r = \frac{v_r}{v}, \tilde{v}_\theta = \frac{v_\theta}{v},$$
$$\tilde{\rho} = \frac{\rho}{\rho_0}, \tilde{p} = \frac{p}{\rho_0 v^2}, \tilde{c} = \frac{c}{c_0},$$
$$\tilde{E}_r = \frac{E_r}{E_0}, \tilde{E}_\theta = \frac{E_\theta}{E_0}, \tilde{B}_z = \frac{B_z}{B_0}.$$

Dimensionless Parameters

The nondimensional parameters governing the flow are defined as follows:

Reynolds number

$$\mathrm{Re} = \frac{\rho_0 v l}{\mu},$$

Peclet number

$$\mathrm{Pe} = \frac{vl}{D},$$

Magnetic interaction parameter (Lorentz force parameter)

$$M = \frac{J_0 B_0 l}{\rho_0 v^2},$$

Electric field parameter

$$E_c = \frac{\rho_e E_0 l}{\rho_0 v^2},$$

Chemical reaction rate parameter

$$K_c = \frac{kl}{v}.$$

Here, v_{rp}denotes the Darcy velocity within the porous layer, $k$represents the permeability of the porous medium, and $\mu$is the dynamic viscosity of the fluid. The slip parameter is denoted by α_p, while αcorresponds to the streamwise wave number. The parameter ωrepresents the frequency, $\varepsilon$is the perturbation parameter, and $i$denotes the imaginary unit.

In order to transform the governing equations (2.1)–(2.4) into their nondimensional form, an appropriate set of dimensionless variables is introduced in the following section.

Non-dimensional Governing Equations

Continuity equation

$$\frac{\partial \tilde{\rho}}{\partial \tilde{t}} + \frac{1}{\tilde{r}}\frac{\partial(\tilde{r}\tilde{\rho}\tilde{v}_r)}{\partial \tilde{r}} + \frac{1}{\tilde{r}}\frac{\partial(\tilde{\rho}\tilde{v}_\theta)}{\partial \tilde{\theta}} = 0 \qquad (2.5)$$

Radial momentum equation

$$\tilde{\rho}\left(\frac{\partial \tilde{v}_r}{\partial \tilde{t}} + \tilde{v}_r\frac{\partial \tilde{v}_r}{\partial \tilde{r}} + \frac{\tilde{v}_\theta}{\tilde{r}}\frac{\partial \tilde{v}_r}{\partial \tilde{\theta}} - \frac{\tilde{v}_\theta^2}{\tilde{r}}\right) = -\frac{\partial \tilde{p}}{\partial \tilde{r}}$$
$$+\frac{1}{\mathrm{Re}}\left[\frac{\partial^2 \tilde{v}_r}{\partial \tilde{r}^2} + \frac{1}{\tilde{r}}\frac{\partial \tilde{v}_r}{\partial \tilde{r}} - \frac{\tilde{v}_r}{\tilde{r}^2} + \frac{1}{\tilde{r}^2}\frac{\partial^2 \tilde{v}_r}{\partial \tilde{\theta}^2} - \frac{2}{\tilde{r}^2}\frac{\partial \tilde{v}_\theta}{\partial \tilde{\theta}}\right]$$
$$+E_c\tilde{E}_r + M\tilde{J}_\theta\tilde{B}_z - \dot{G}\,\frac{\tilde{\rho}}{\tilde{r}^2}\sin\theta \qquad (2.6)\text{where}$$

$$\dot{G} = \frac{GM}{v^2 l^2}.$$

Azimuthal momentum equation

$$\tilde{\rho}\left(\frac{\partial \tilde{v}_\theta}{\partial \tilde{t}} + \tilde{v}_r\frac{\partial \tilde{v}_\theta}{\partial \tilde{r}} + \frac{\tilde{v}_\theta}{\tilde{r}}\frac{\partial \tilde{v}_\theta}{\partial \tilde{\theta}} + \frac{\tilde{v}_r\tilde{v}_\theta}{\tilde{r}}\right) = -\frac{1}{\tilde{r}}\frac{\partial \tilde{p}}{\partial \tilde{\theta}}$$
$$+\frac{1}{\mathrm{Re}}\left[\frac{\partial^2 \tilde{v}_\theta}{\partial \tilde{r}^2} + \frac{1}{\tilde{r}}\frac{\partial \tilde{v}_\theta}{\partial \tilde{r}} - \frac{\tilde{v}_\theta}{\tilde{r}^2} + \frac{1}{\tilde{r}^2}\frac{\partial^2 \tilde{v}_\theta}{\partial \tilde{\theta}^2} + \frac{2}{\tilde{r}^2}\frac{\partial \tilde{v}_r}{\partial \tilde{\theta}}\right]$$
$$+\dot{G}\,\frac{\tilde{\rho}}{\tilde{r}^2}\cos\theta \qquad (2.7)$$

Impurity concentration (reaction–diffusion) equation

$$\frac{\partial \tilde{c}_i}{\partial \tilde{t}} + \tilde{v}_r\frac{\partial \tilde{c}_i}{\partial \tilde{r}} + \frac{\tilde{v}_\theta}{\tilde{r}}\frac{\partial \tilde{c}_i}{\partial \tilde{\theta}} = \frac{1}{\mathrm{Pe}}\left[\frac{1}{\tilde{r}}\frac{\partial}{\partial \tilde{r}}\left(\tilde{r}\frac{\partial \tilde{c}_i}{\partial \tilde{r}}\right) + \frac{1}{\tilde{r}^2}\frac{\partial^2 \tilde{c}_i}{\partial \tilde{\theta}^2}\right] - K_c\tilde{c}_i \qquad (2.8)$$

3. METHOD OF SOLUTION

The velocity field and plasma–dust concentration are analyzed using the perturbation method. In this approach, each flow variable is decomposed into two parts: a steady base-state component, represented by uppercase symbols, and a small two-dimensional linear perturbation component, denoted by a tilde (̃,). The perturbation is assumed to propagate in the radial direction with a harmonic dependence on space and time.

Accordingly, the flow variables are expressed as:

$$v_r(r,\theta,t) = V_{rB}(\theta) + \varepsilon\,\tilde{v}_r(\theta)\,e^{i(\alpha r+\omega t)} + O(\varepsilon^2), \qquad (3.9)$$
$$v_\theta(r,\theta,t) = V_{\theta B}(\theta) + \varepsilon\,\tilde{v}_\theta(\theta)\,e^{i(\alpha r+\omega t)} + O(\varepsilon^2), \qquad (3.10)$$
$$p(r,\theta,t) = p_B(\theta) + \varepsilon\,\tilde{p}(\theta)\,e^{i(\alpha r+\omega t)} + O(\varepsilon^2), \qquad (3.11)$$
$$c_i(r,\theta,t) = C_{iB}(\theta) + \varepsilon\,\tilde{c}_i(\theta)\,e^{i(\alpha r+\omega t)} + O(\varepsilon^2). \qquad (3.12)$$

Here, V_{rB}, $V_{\theta B}$, p_B, and C_{iB}denote the base-state (steady) solutions, while $\tilde{v}_r$, $\tilde{v}_\theta$, $\tilde{p}$, and $\tilde{c}_i$represent the corresponding perturbation amplitudes. The parameter $\varepsilon \ll 1$is the perturbation parameter, $\alpha$is the streamwise wave number, $\omega$is the frequency of oscillation, and $i$denotes the imaginary unit.

Substituting these decomposed forms into the nondimensional governing equations (2.6)–(2.8), and assuming steady base flow, the equations are separated into base-state and perturbation components. By retaining only the first-order terms in the perturbation parameter ε, a coupled system of linearized differential equations governing the perturbation quantities is obtained. The base-state equations are solved analytically, while the perturbation equations are solved numerically subject to the prescribed boundary conditions.

Base Part Equations

Under the assumption of steady flow, the time-dependent terms and perturbation components are neglected, and only the leading-order $O(1)$terms are retained. Consequently, the governing equations reduce to a set of ordinary differential equations

describing the base-state flow variables, which depend only on the angular coordinate $\tilde{\theta}$.

The nondimensional base-state radial momentum equation is given by

$$\frac{\partial^2 \tilde{V}_{rB}}{\partial \tilde{\theta}^2} - \mathrm{Re}\,\dot{G}\,\tilde{\rho}\sin\,\theta - \mathrm{Re}\,\tilde{r}^2\frac{\partial \tilde{p}}{\partial \tilde{r}} + \mathrm{Re}\,\tilde{r}^2 E_c \tilde{E}_r + \mathrm{Re}\,\tilde{r}^2 M \tilde{J}_\theta \tilde{B}_z \partial \tilde{\theta} 0, \qquad (4.13)$$

The nondimensional base-state azimuthal momentum equation takes the form

$$\frac{\partial^2 \tilde{V}_{\theta B}}{\partial \tilde{\theta}^2} - \mathrm{Re}\,\tilde{r}\frac{\partial \tilde{p}}{\partial \tilde{\theta}} + \mathrm{Re}\,\dot{G}\cos\,\theta = 0, \qquad (4.14)$$

The base-state impurity concentration equation is governed by the reaction–diffusion balance

$$\frac{\partial^2 \tilde{C}_{iB}}{\partial \tilde{\theta}^2} - K_c\,\mathrm{Pe}\,\tilde{r}^2 \tilde{C}_{iB} = 0. \qquad (4.15)$$

Remarks on the Base Flow

Here, $\tilde{V}_{rB}$, $\tilde{V}_{\theta B}$, and $\tilde{C}_{iB}$denote the base-state radial velocity, azimuthal velocity, and impurity concentration, respectively. The gravitational parameter $\dot{G}$represents the nondimensional gravitational strength, while $E_c$and Mquantify the effects of electric and magnetic fields. These equations describe the steady angular structure of the accretion flow under the combined influence of gravity, electromagnetic forces, viscosity, and chemical reactions.

Perturbed Part Equations

The linearized perturbation equations governing the azimuthal velocity, radial velocity, and concentration fields are given as follows.

(i) Azimuthal Velocity Perturbation Equation

$$\frac{\partial^2 \tilde{v}_\theta}{\partial \tilde{\theta}^2} + \tilde{v}_\theta[Re\,\tilde{r}^2\tilde{\rho}a_4 + Re\,\tilde{r}^2\tilde{\rho}a_3\left(\frac{k}{2}\tilde{\theta}^2 + c_1\tilde{\theta}\right) + Re\,\tilde{r}\tilde{\rho} + \left(\frac{k}{2}\tilde{\theta}^2 + c_1\tilde{\theta}\right)Re\,\tilde{r}\tilde{\rho} - \alpha^2\tilde{r} - 1] - \tilde{\rho}Re\,\tilde{r}^2(D\tilde{\theta} + c_3)\text{prescribed boundary conditions.} \qquad (5.16)$$

(ii) Radial Velocity Perturbation Equation

$$\frac{\partial^2 \tilde{v}_r}{\partial \tilde{\theta}^2} + \tilde{v}_r[Re\,\tilde{r}^2\tilde{\rho}a_4 + Re\,\tilde{r}^2 a_3\left(\frac{k}{2}\tilde{\theta}^2 + c_1\tilde{\theta} + c_2\right) - \alpha^2\tilde{r}^2 - a_3\tilde{r} - 1]$$
$$-\tilde{\rho}Re\,\tilde{r}\left(D\tilde{\theta}^2 + c_3\tilde{\theta} + c_4\right)[1 - \left(D\tilde{\theta}^2 + c_3\tilde{\theta} + c_4\right)] + \tilde{\rho}Re\,\tilde{r}^2 a_3 - 2 - \tilde{\rho}Re\,\tilde{r}^2(k\tilde{\theta} + c_1) = 0 \qquad (5.17)$$

(iii) Concentration Perturbation Equation

$$\frac{\partial^2 \tilde{c}_i}{\partial \tilde{\theta}^2} + \tilde{c}_i[Pe\,\tilde{r}^2 a_4 + Pe\,\tilde{r}^2 a_3\left(\frac{k}{2}\tilde{\theta}^2 + c_1\tilde{\theta}\right) - \tilde{r}^2\alpha^2 - k_c]$$
$$-Pe\,\tilde{r}\left(D\tilde{\theta}^2 + c_3\tilde{\theta}\right)\left(\frac{\gamma\cosh(\gamma\tilde{\theta})}{\sinh(2\pi\gamma)}\right) = 0 \qquad (5.18)$$

Parameter Definition

$$\gamma = \tilde{r}\sqrt{k_c Pe}$$

Base Part Boundary Conditions

The boundary conditions corresponding to the base flow are prescribed as

$$\tilde{V}_{rB} = 0, \tilde{C}_{Bi} = 0 \text{at } \tilde{\theta} = 0$$
$$\frac{\partial \tilde{V}_{rB}}{\partial \tilde{\theta}} = -\alpha\sigma(\tilde{V}_{rB} - \tilde{V}_{rpB}), \text{at } \tilde{\theta} = 2\pi$$
$$\frac{\partial \tilde{V}_{rB}}{\partial \tilde{\theta}} = \alpha\sigma(\tilde{V}_{rB} - \tilde{V}_{rpB}), \text{at } \tilde{\theta} = -2\pi$$
$$\tilde{C}_{Bi} = 1 \text{at } \tilde{\theta} = 2\pi$$

Perturbed Part Boundary Conditions

The corresponding boundary conditions for the perturbed flow variables are

$$\tilde{v}_r = 0, \tilde{v}_\theta = 0, \tilde{c}_i = 1 \text{at } \tilde{\theta} = 0$$
$$\frac{\partial \tilde{v}_r}{\partial \tilde{\theta}} = -\alpha\sigma(\tilde{v}_r - \tilde{v}_{rp}), \text{at } \tilde{\theta} = 2\pi$$
$$\frac{\partial \tilde{v}_r}{\partial \tilde{\theta}} = \alpha\sigma(\tilde{v}_r - \tilde{v}_{rp}), \text{at } \tilde{\theta} = -2\pi$$

Base Part Solutions

The analytical solutions of the base flow equations are obtained as

$$\tilde{V}_{rB}(\theta) = \frac{k}{2}\theta^2 + c_1\theta + c_2$$
$$\tilde{V}_{\theta B}(\theta) = \frac{D}{2}\theta^2 + c_3\theta + c_4$$

where the constants are given by

$$c_1 = \frac{1 - k\,2\pi^2}{2\pi}, c_2 = 0, c_4 = 0, c_3 = \frac{1 - D\,2\pi^2}{2\pi}$$

The auxiliary parameters are defined as

$$a_3 = \alpha\tan(\alpha r + \omega t), a_4 = \omega\tan(\alpha r + \omega t)$$
$$k = Re\left(\dot{G}\sin\,\theta\,\tilde{\rho} + \tilde{r}^2\frac{\partial \tilde{p}}{\partial \tilde{r}} - \tilde{r}^2 E_c \tilde{E}_r - M\tilde{r}^2\tilde{J}_\theta\tilde{B}_z\right)$$
$$D = Re\left(\tilde{r}\frac{\partial \tilde{p}}{\partial \tilde{\theta}}\right) - Re\dot{G}\cos\,\theta$$

The constants $c_1, c_2, c_3, c_4$are evaluated using the $2\tilde{r}^2 2(k\tilde{\theta} + c_1) = 0$

Plasma and Dust Concentration Dynamics

(Chemical reaction present, $K_c \neq 0$)

The solution for the base concentration perturbation $\tilde{C}_{B1}$is assumed in the form

$$\tilde{C}_{B1} = Ae^{\gamma\theta} + Be^{-\gamma\theta}$$

Applying the boundary conditions, we obtain

$$A = -B, A = \frac{1}{2\sinh(2\pi\gamma)}$$

with

$$\gamma^2 = K_c Pe\,\tilde{r}^2 > 0$$

Concentration Perturbation Equation

$$\frac{\partial^2 \tilde{c}_i}{\partial \tilde{\theta}^2} + \tilde{c}_i[Pe\,\tilde{r}^2 a_4 + Pe\,\tilde{r}^2 a_3\left(\frac{k}{2}\theta^2 + c_1\theta\right) - \tilde{r}^2\alpha^2 - k_c] - Pe\,\tilde{r}\left(\frac{D}{2}\theta^2 + c_3\theta\right)\frac{\partial \tilde{C}_{B1}}{\partial \tilde{\theta}} = 0 \qquad (5.19)$$

where

$$\frac{\partial \tilde{C}_{B1}}{\partial \tilde{\theta}} = \left(\frac{\gamma \cosh(\gamma\theta)}{\sinh(2\pi\gamma)}\right)$$

Numerical Solution and Discussion

The perturbed equations are solved numerically under the prescribed boundary conditions using **MATLAB**. Graphical results are presented to illustrate the variation of axial velocity and plasma (dust) concentration for different values of the chemical reaction parameter C_1.

4. RESULTS AND DISCUSSION

Velocity Graphs

Figure 2. illustrates the variation of azimuthal velocity, radial velocity, and plasma concentration around the accretion disk under perturbed flow conditions. The azimuthal velocity represents the rotational response of the flow to viscous effects, magnetic interaction, and geometric constraints. The radial velocity indicates the strength of inward or outward motion influenced by slip conditions, electromagnetic forces, and the underlying base flow structure. The concentration profile reflects the combined effects of diffusion, advection, and chemical reactions within the disk. Collectively, these results demonstrate the evolution of perturbations and highlight how viscosity, magnetic forces, and reaction dynamics jointly influence the stability and transport mechanisms in the accretion flow.

Figure 3. shows that increasing magnetic and electric forces suppress the azimuthal velocity, leading to a reduction in flow strength and a smoother velocity profile. This behavior arises from enhanced electromagnetic damping, which resists rotational motion in the plasma.

Figure 4. presents the variation of radial velocity for different values of the Hartmann number and electric number. The results indicate that the radial velocity decreases as either parameter increases, since stronger magnetic and electric effects oppose the inward motion driven by gravity. The angular variation of the velocity remains approximately sinusoidal due to the gravitational contribution. Overall, higher electromagnetic strength results in weaker inflow and reduced accretion rates.

Figure 5. demonstrates the influence of the Hartmann number on the azimuthal perturbation velocity. An increase in the Hartmann number strengthens the magnetic field, thereby enhancing Lorentz braking and reducing the azimuthal velocity around the disk. The Beavers–Joseph slip condition accounts for partial slip at the disk surface, and the results clearly show how magnetic damping modifies the angular flow pattern within the accretion disk.

Figure 6. highlights the competing effects of gravity and electromagnetic forces on the radial velocity. While gravity enhances the radial inflow, magnetic and electric forces act in opposition, reducing the magnitude of the radial velocity and stabilizing the flow.

Figure 7. examines the effect of the gravity parameter Gon the azimuthal (rotational) velocity of the plasma. Gravity introduces a sinusoidal forcing in the angular direction, which tends to distort the rotational flow. In contrast, the magnetic field (Hartmann number), electric effects, and Beavers–Joseph slip condition provide damping that resists this motion. The numerical solution of the governing differential equation over the angular domain $0 \le \theta \le \pi$ reveals that increasing gravity strengthens the angular variation of the velocity, whereas magnetic and electric effects suppress and smooth the rotational profile.

Figure 8. illustrates the effect of gravitational strength on the dust and plasma concentration within the accretion disk. As gravity increases, the inward attractive force acting on both the plasma and suspended dust particles becomes stronger. This enhanced gravitational pull accelerates the radial inflow and compresses the spatial distribution of the transported species. Consequently, the concentration profiles become steeper, boundary layers become thinner, and the impurity distribution becomes increasingly localized near the accreting region.

Figure 9. demonstrates the influence of the electric field on particle concentration. An increase in the electric field parameter $E_c$induces stronger electric drift, leading to a redistribution of particles along the disk. This results in sharper concentration gradients and a noticeable shift in the location of peak concentration, indicating enhanced electromigration effects on the charged species.

Figure 10. presents the combined effects of the Hartmann number $M$and the electric field parameter $E_c$on concentration dynamics. The Hartmann number contributes to magnetic damping, which stabilizes and smooths the concentration profile by suppressing fluctuations. In contrast, the electric field tends to shift

and distort the concentration through electric drift. The interplay between magnetic stabilization and electric redistribution governs the overall shape and smoothness of the concentration variation along the azimuthal direction.

Figures 11-16. illustrate how electromagnetic forces, gravity, viscous stresses, and impurity effects collectively govern the two-dimensional accretion flow. The radial inflow primarily determines the accretion rate, while the azimuthal motion controls angular-momentum transport within the disk. Impurity transport modifies the local density and mass flux, thereby influencing the overall rate of accretion. The Hartmann number and Electric field number regulate the relative strengths of magnetic and electric forces and their impact on the flow dynamics.

The accretion-rate analysis quantifies the rate at which mass is transported inward through the disk as a result of viscous stresses, magnetic and electric forces, gravitational attraction, and impurity loading. The radial velocity governs the local mass flux, whereas azimuthal motion facilitates angular-momentum loss, enabling matter to spiral toward the black hole. An increase in impurity concentration enhances the effective density of the flow, thereby strengthening the inward mass transport. By integrating the radial mass flux over the full azimuthal direction, the accretion rate at a given radius is obtained, allowing identification of regions where mass transport is efficient and regions where magnetic, electric, or chemical effects suppress inflow. Overall, the results demonstrate how the coupled effects of magnetohydrodynamic forces and impurity dynamics regulate the total mass accreted by the central black hole.

The accretion rate $\dot{M}$is calculated as

$$\dot{M}(r) = \int_0^{2\pi} \rho\,(1+\beta_c c_i)\,\tilde{V}_r(\theta)\,d\theta.$$

Figure 17. illustrates the formation of shock-like structures in regions where the radial inflow undergoes rapid deceleration. These shocks arise due to a sudden imbalance between the inward gravitational driving force and the opposing viscous, magnetic, and electric resistances. An increase in gravitational strength enhances the intensity of the radial inflow, leading to stronger and sharper shock structures. In contrast, magnetic fields and impurity loading modify the effective inertia and introduce additional resistance, which alters both the location and sharpness of the shocks within the accretion disk.

Figure 18. demonstrates that the accretion process is governed by a delicate balance between driving forces, such as gravity and pressure gradients, and resisting mechanisms, including viscous stresses, Lorentz forces, and impurity-induced drag. Shock formation signifies a sudden reorganization of the flow, where kinetic energy is rapidly redistributed and dissipated. Variations in gravitational strength, magnetic field intensity, and impurity concentration significantly influence the position, strength, and structure of these shocks. The results highlight the important role of shock dynamics in regulating mass transport, energy dissipation, and overall stability of the accretion flow.

Figure 19. illustrates the formation of jets in a two-dimensional viscous magnetohydrodynamic accretion flow in the presence of dust impurities. The results demonstrate that the combined action of gravitational, electric, and magnetic forces governs the radial inflow, angular momentum transport, impurity redistribution, and the emergence of collimated outflows. The interaction between the Lorentz force and rotational motion generates favorable conditions for jet launching along preferred directions.

The strength and structure of the jet are strongly influenced by key dimensionless parameters. An increase in the Hartmann number enhances magnetic confinement and collimation of the jet, while the electric field strength modifies particle drift and charge separation, thereby affecting jet acceleration. The Reynolds number controls the relative importance of inertial and viscous forces, determining the efficiency of angular momentum transport necessary for jet formation. The Peclet number regulates impurity transport through advection and diffusion, and the chemical reaction rate constant alters the local concentration of impurities, which in turn modifies the effective density and momentum balance of the flow.

Overall, the model reveals that jet formation is a natural consequence of the coupled magnetohydrodynamic and impurity dynamics in black hole accretion flows. The results provide insight into how electromagnetic forces, gravity, and chemical processes jointly regulate both the accretion rate onto the black hole and the strength of the associated astrophysical jets.

Figures 20-23. present the influence of gravity on the two-dimensional plasma–impurity accretion flow. The computed solutions clearly demonstrate that gravity plays a dominant regulatory role in shaping the overall accretion dynamics. As the gravitational parameter increases, the inward radial force is significantly intensified, resulting in steeper radial velocity gradients and a pronounced acceleration of the inflow toward the central black hole.

This enhanced radial convergence alters the angular momentum balance of the system. The stronger inward pull reduces the azimuthal velocity by redistributing angular momentum more efficiently, thereby weakening the rotational support of the accretion disk. Consequently, the disk structure becomes more radially dominated, favouring accretion rather than sustained rotation.

Gravity also has a substantial impact on the impurity concentration field. With increasing gravitational strength, the plasma–dust mixture becomes more stratified, and contaminants are increasingly confined toward the inner radial regions of the disk. This behavior arises from gravitational focusing combined with a reduction in outward diffusive transport, which limits the spread of impurities across the disk.

The combined modification of radial velocity, azimuthal shear, and impurity distribution leads to a net enhancement of the accretion rate. As the magnitude of the inward radial velocity increases, the mass flux toward the black hole grows correspondingly. Overall, the present model highlights gravity as a fundamental physical driver that governs inflow strength, rotational shear, impurity accumulation, and ultimately the efficiency of mass accretion in plasma–dust accretion systems around black holes.

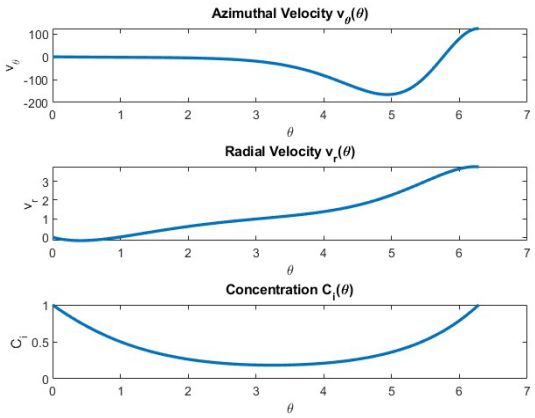

Figure 2 : Azimuthal velocity, Radial Velocity and Concentration

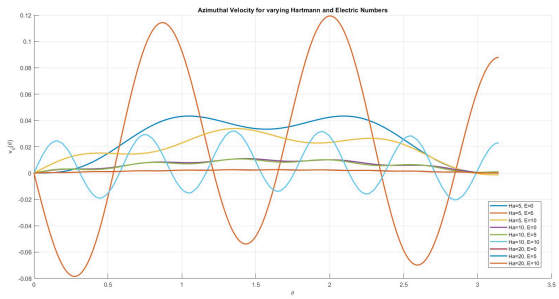

Figure 3:Azimuthal Velocity for varying Hartmann Number and Electric
Number

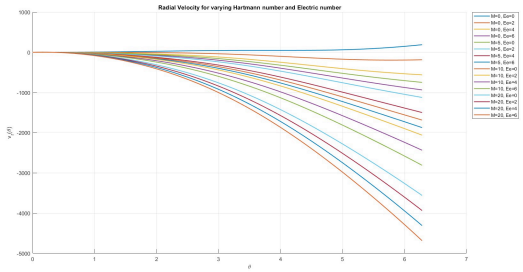

Figure 4: Radial Velocity for varying Hartmann and Electric number

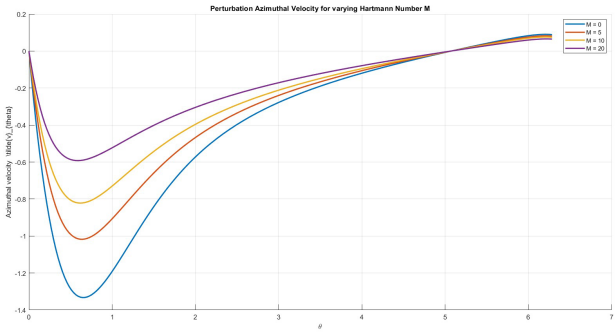

Figure 5 :Peturbation Azimuthal Velocity for Varying Hartman Number

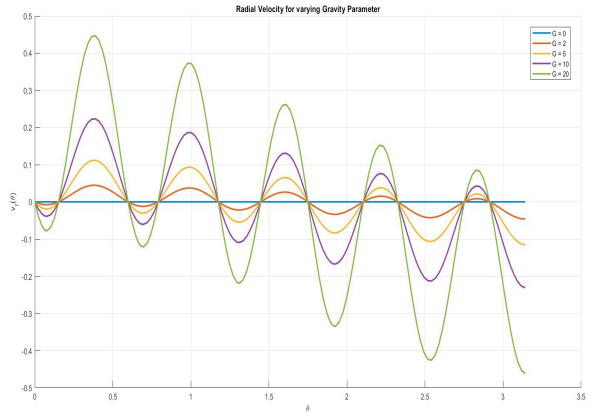

Figure 6 :Radial Velocity for varying Gravity parameter

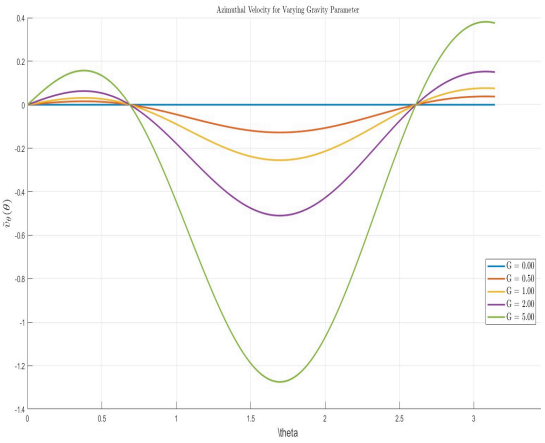

Figure 7: Azimuthal Velocity for Varying Gravity parameter

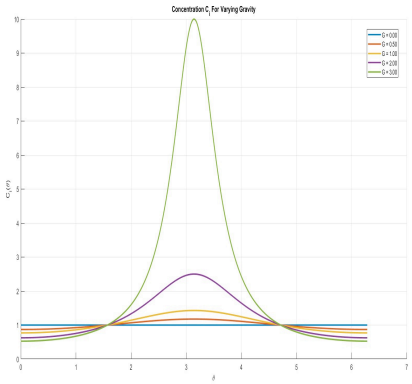

Figure 8 :Concentration for varying Gravity

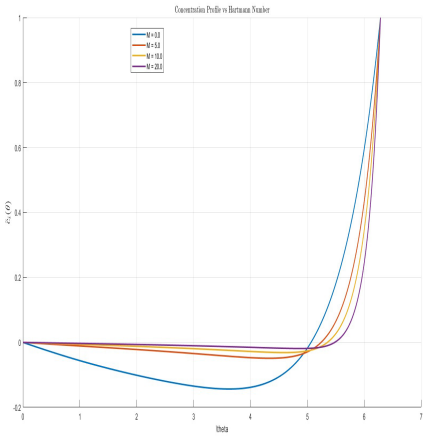

Figure 9 : Concentration profile vs Hartmann Number

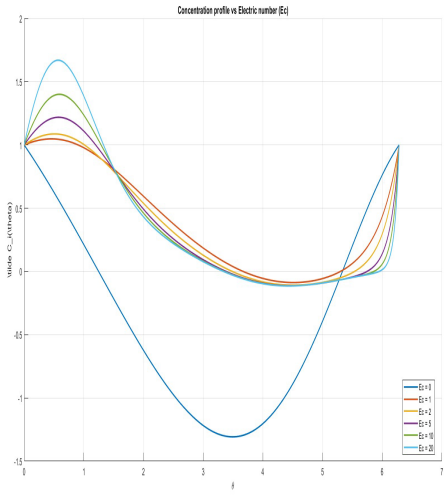

Figure 10 : Concentration profile vs Electric number

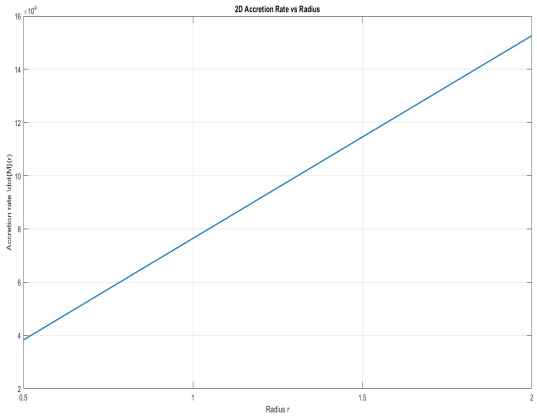

Figure 11 : Accretion rate vs Radius

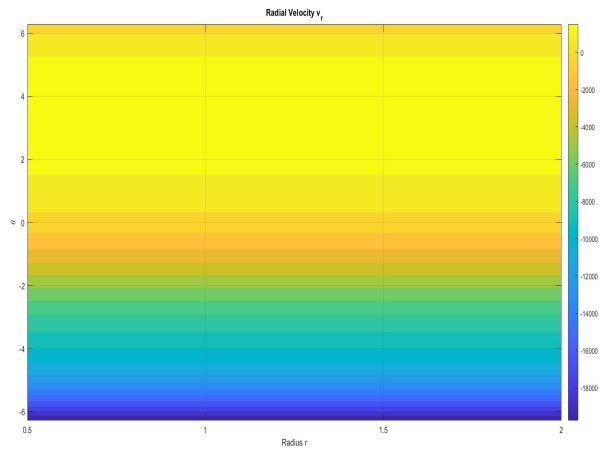

Figure 12: Acceration rate for Radial Velocity

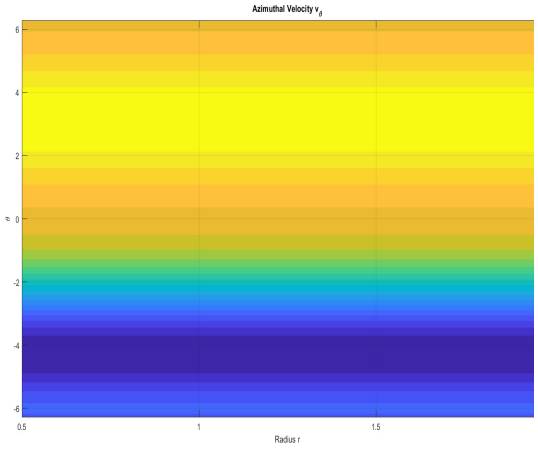

Figure 13 : Accretion rate for Azimuthal velocity

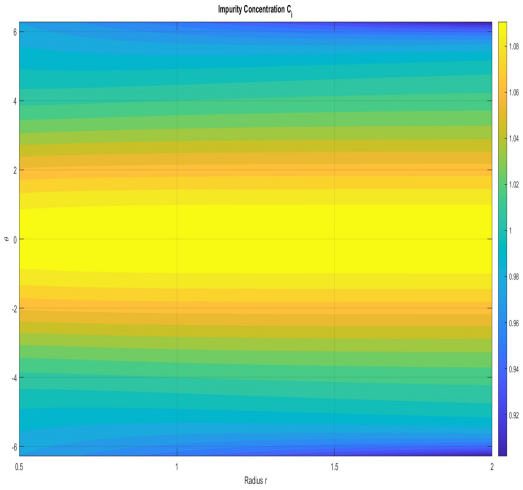

Figure 14 : Accretion rate for Impurity Concentration

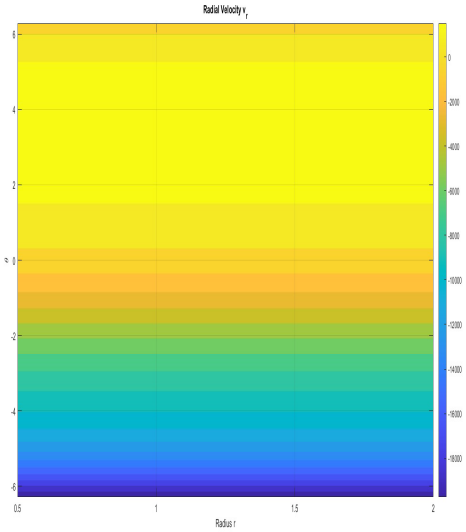

Figure 15 :Accretion rate for Radial Velocity

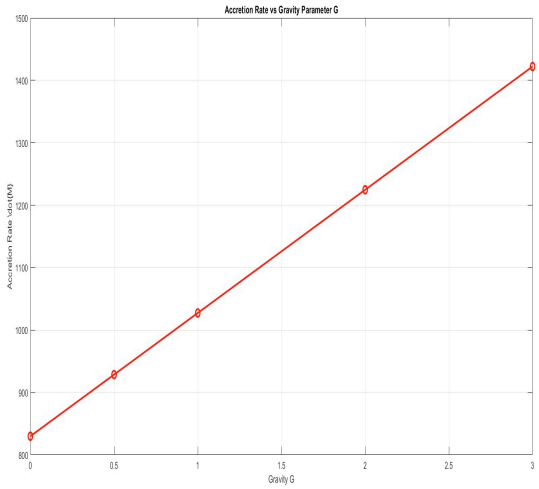

Figure 16:Accretion Rate vs Gravity Parameter

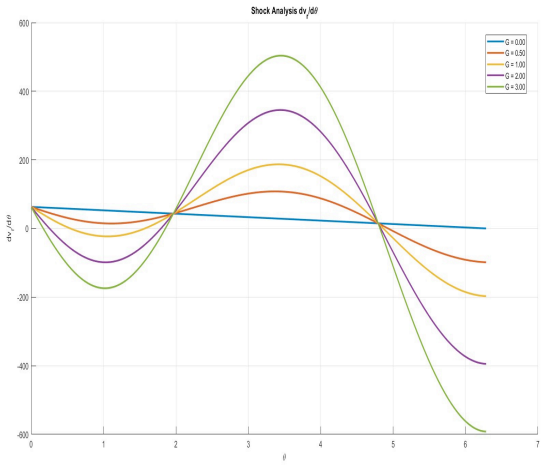

Figure 17 : Shock analysis for Radial Velocity

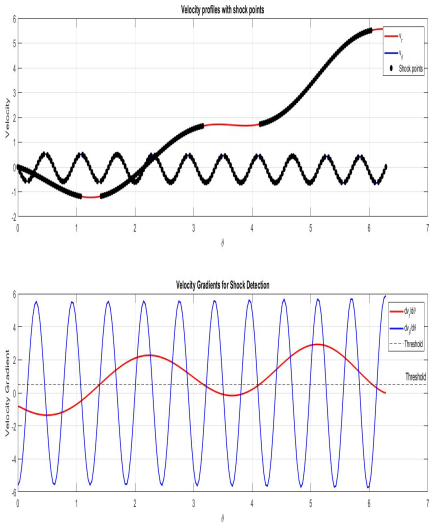

Figure 18: Velocity profiles with Shock point and Velocity Gradient for
Shock Detection

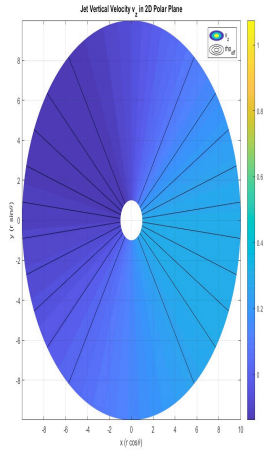

Figure 19 : Jet vertical Velocity

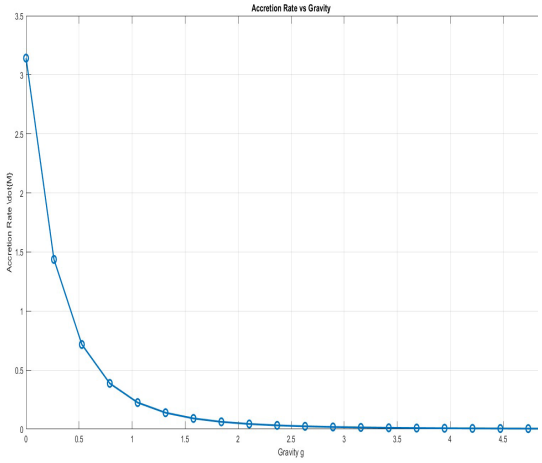

Figure 20 : Accretion Rate vs Gravity

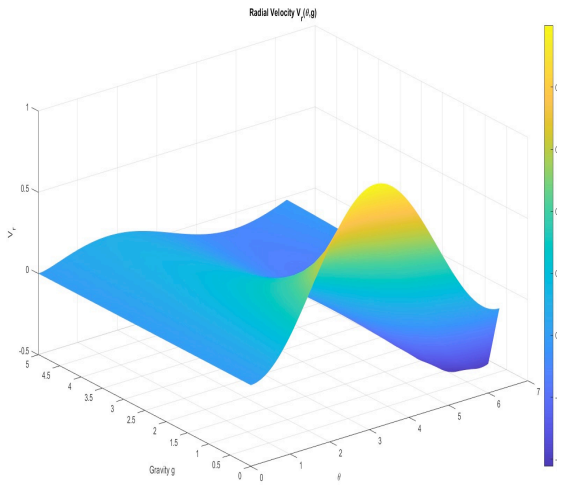

Figure 21:Radial Velocity vs Gravity

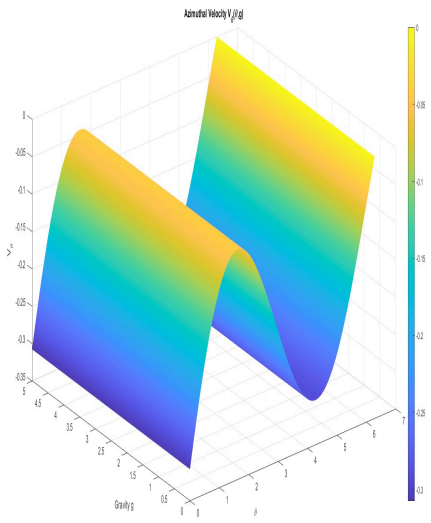

Figure 22 : Azimuthal Velocity vs Gravity

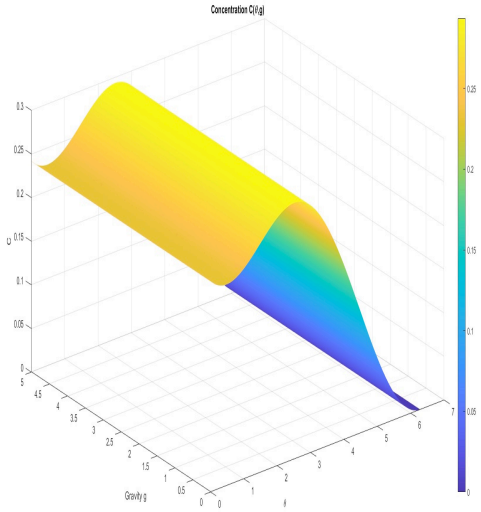

Figure 23 : Concentration vs Gravity

5.CONCLUSION

A 2D viscous MHD accretion model with gravity, electric and magnetic fields, and impurities is analyzed using perturbation theory. Gravity enhances radial inflow and accretion, while magnetic and electric fields suppress velocities through Lorentz damping. Impurities and chemical reactions modify concentration and mass transport. The coupled effects

produce shocks, reconnection regions, and jet formation, demonstrating how MHD forces and impurities jointly control black hole accretion dynamics.

References

1. Balbus, S. A., & Hawley, J. F. (1998). Instability, turbulence, and transport in accretion disks. *Reviews of Modern Physics*, **70**, 1–53.
2. Shakura, N. I., &Sunyaev, R. A. (1973). Black holes in binary systems: Observational appearance. *Astronomy and Astrophysics*, **24**, 337–355.
3. Kato, S., Fukue, J., &Mineshige, S. (2008). *Black-Hole Accretion Disks*. Kyoto: Kyoto University Press.
4. Chakrabarti, S. K. (1996). Accretion processes on a black hole. *Physics Reports*, **266**, 229–390.
5. Koide, S., Shibata, K., & Kudoh, T. (1999). Relativistic MHD simulations of jet formation. *The Astrophysical Journal*, **522**, 727–752.
6. Ghosh, S., & Chakrabarti, S. K. (2018). Two-dimensional disc accretion with angular momentum transport. *Monthly Notices of the Royal Astronomical Society*, **479**, 121–134.
7. Frank, J., King, A., & Raine, D. (2002). *Accretion Power in Astrophysics*. Cambridge: Cambridge University Press.
8. Laibe, G., & Price, D. J. (2012). Dust–gas dynamics in two-fluid MHD discs. *Monthly Notices of the Royal Astronomical Society*, **420**, 2345–2364.
9. Tsuribe, T., & Umemura, M. (1997). Nonlinear evolution of self-gravitating disks. *The Astrophysical Journal*, **486**, 48–64.
10. Matarrese, S., &Mohayaee, R. (2002). Dynamics of dust in astrophysical plasmas. *Monthly Notices of the Royal Astronomical Society*, **329**, 37–48.
11. Shu, F. H. (1992). *The Physics of Astrophysics, Vol. II: Gas Dynamics*. Mill Valley: University Science Books.
12. Goedbloed, J. P., Keppens, R., &Poedts, S. (2019). *Magnetohydrodynamics of Plasmas*. Cambridge: Cambridge University Press.
13. Parker, E. N. (2007). *Electric and Magnetic Fields in the Cosmos*. Princeton: Princeton University Press.
14. Choudhuri, A. R. (1998). *The Physics of Fluids and Plasmas*. Cambridge: Cambridge University Press.
15. Beavers, G. S., & Joseph, D. D. (1967). Boundary conditions at a permeable wall. *Journal of Fluid Mechanics*, **30**, 197–207.
16. Whitaker, S. (1999). *The Method of Volume Averaging*. Dordrecht: Kluwer Academic Publishers.
17. Murray, J. D. (2003). *Mathematical Biology II: Spatial Models and Biomedical Applications*. New York: Springer.
18. Pandey, B. P., & Vladimirov, S. V. (2007). Dusty plasma dynamics. *Physics of Plasmas*, **14**, 103703.
19. Shadmehri, M. (2004). Cooling, viscosity, and magnetic fields in accretion flows. *The Astrophysical Journal*, **612**, 1000–1008.
20. Bisnovatyi-Kogan, G. S., & Lovelace, R. V. (2001). Magnetic fields and disk structure. *New Astronomy Reviews*, **45**, 663–680.
21. Nayfeh, A. H. (1973). *Perturbation Methods*. New York: Wiley.
22. Bender, C. M., & Orszag, S. A. (1999). *Advanced Mathematical Methods for Scientists and Engineers*. New York: Springer.